International Journal of Heat and Mass Transfer 61 (2013) 293–309

Contents lists available at SciVerse ScienceDirect

International Journal of Heat and Mass Transfer

journal homepage: www.elsevier.com/locate/ijhmt

Experimental and theoretical investigation of annular flow condensation in microgravity

Hyoungsoon Lee [a], Issam Mudawar [a,*], Mohammad M. Hasan [b]

[a] Boiling and Two-Phase Flow Laboratory (BTPFL), School of Mechanical Engineering, Purdue University, 585 Purdue Mall, West Lafayette, IN 47907, USA
[b] NASA Glenn Research Center, 21000 Brookpark Road, Cleveland, OH 44135, USA

ARTICLE INFO

Article history:
Received 9 January 2013
Received in revised form 24 January 2013
Accepted 1 February 2013
Available online 5 March 2013

Keywords:
Microgravity
Condensation
Annular flow

ABSTRACT

Vehicles for future manned space missions will demand unprecedented increases in power requirements and heat dissipation. Achieving these goals while maintaining acceptable size and weight limits will require replacing present single-phase thermal management components with far more efficient two-phase counterparts. This study discusses the development of an experimental facility for the study of annular condensation of FC-72 in microgravity, which was tested in parabolic flight as a prelude to the development of NASA's Flow Boiling and Condensation Experiment (FBCE) for the International Space Station (ISS). The flow behavior of the condensate film is shown to be sensitive mostly to the mass velocity of FC-72, with low mass velocities yielding laminar flow with a smooth interface, and high mass velocities turbulent flow with appreciable interfacial waviness. A select number of tests repeated in microgravity, Lunar gravity and Martian gravity prove that the influence of gravity is very pronounced at low mass velocities, manifest by circumferential uniformity for microgravity versus appreciable thickening along one side of the condensation tube for Lunar and Martian conditions. However, the thickening is nonexistent for Lunar and Martian conditions at high mass velocities due to increased vapor shear on the film interface, proving high mass velocity is an effective means to negating the influence of gravity in space missions. For microgravity, the condensation heat transfer coefficient is highest near the inlet, where the film is both thin and laminar, and decreases along the condensation length, but increases again downstream for high mass velocities due to turbulence and increased waviness. A model is proposed to predict the condensation heat transfer which accounts for dampening of turbulent fluctuations near the film interface. The model shows good agreement with the heat transfer coefficient data in both trend and magnitude.

1. Introduction

1.1. Importance of two-phase thermal management to future space missions

Future space missions to Mars and beyond are challenging all present practices in the design of space vehicles. These missions are expected to greatly increase in scope, size, complexity and duration. They will also bring about unprecedented increases in both power requirements and heat dissipation demands. However, it is highly unlikely that these increases can be accomplished with a commensurate increase in the size and weight of vehicle sub-systems, given the enormous impact of these two parameters on vehicle cost. Space vehicle developers are therefore exploring more efficient designs with greater power-to-weight ratio, including the use of fission power and replacing present single-phase thermal management systems with two-phase counterparts [1–6].

The effectiveness of two-phase thermal management systems is derived mostly from the orders-of-magnitude enhancement in evaporation and condensation heat transfer coefficients compared to single-phase counterparts. Thermal management is achieved via a Thermal Control System (TCS) that is tasked with heat acquisition, transport and rejection in the space vehicle. In a two-phase TCS, heat acquisition from a variety of heat-dissipating sources is achieved by evaporation or flow boiling of a working fluid. The heat is ultimately rejected to deep space to condense the working fluid back to liquid state. The heat acquisition can be achieved in a variety of boiling schemes including pool boiling [7,8], channel flow boiling [9–11], jet [12–14], and spray [15,16], especially when implemented with surface enhancement [17–19]. However, the configuration most suitable to a space vehicle's TCS is flow boiling in tubes. Similarly, the most suitable condensation configuration is flow condensation in tubes.

* Corresponding author. Tel.: +1 765 494 5705; fax: +1 765 494 0539.
E-mail address: mudawar@ecn.purdue.edu (I. Mudawar).
URL: https://engineering.purdue.edu/BTPFL (I. Mudawar).

0017-9310/$ - see front matter © 2013 Elsevier Ltd. All rights reserved.
http://dx.doi.org/10.1016/j.ijheatmasstransfer.2013.02.010

Nomenclature

A	area
$A_{f,*}$	cross-section area of liquid control volume
A^+	parameter in eddy diffusivity model
c_p	specific heat at constant pressure
D_i	inner diameter of condensation tube
D_o	outer diameter of condensation tube
f_i	interfacial friction factor
G	mass velocity of FC-72
g_e	Earth's gravitational acceleration
G_w	mass velocity of water
h	local condensation heat transfer coefficient
h_{fg}	latent heat of vaporization
K	Von-Karman constant
k	thermal conductivity
$\dot{m}$	mass flow rate
$\dot{m}_w$	mass flow rate for water
P	pressure
P_f	perimeter
Pr	Prandtl number
Pr_T	turbulent Prandtl number
q	heat transfer rate
q''	heat flux
Re	Reynolds number
T	temperature
t	time
u	axial velocity
u^+	dimensionless axial velocity
u^*	friction velocity
W	outer channel width of condensation module CM-FV
x_e	thermodynamic equilibrium quality
y	distance perpendicular to wall
y^+	dimensionless distance perpendicular to wall
z	stream-wise coordinate

Greek symbols

Γ_{fg}	condensation mass transfer rate per unit axial distance
δ	liquid film thickness
δ^+	dimensionless liquid film thickness
ε_m	eddy momentum diffusivity
μ	dynamic viscosity
ν	kinematic viscosity
ρ	density
τ	shear stress

Subscripts

exp	experimental
f	saturated liquid
FC	FC-72
film	liquid film
g	saturated vapor
i	interfacial; inner surface of condensation tube
in	inlet of condensation length
o	outer surface of condensation tube
pred	predicted
sat	saturation
ss	stainless steel
w	water
wall	wall

A major challenge to designing a fission power system or phase-change TCS for a space vehicle is poor understanding of flow boiling and condensation in reduced gravity. Two-phase transport behavior can be highly susceptible to the influence of buoyancy, which is proportional to the product of gravity and density difference between liquid and vapor. Unfortunately, existing flow boiling and condensation pressure drop and heat transfer correlations and models are derived almost entirely from experiments that have been conducted in Earth's gravity. Therefore, it is impossible to ascertain the validity of these predictive tools for reduced gravity operation, especially microgravity, without conducting validation experiments over the appropriate gravity range. This fact is evident in a 2011 report by the National Research Council (NRC) [20] that was submitted to the U.S. Congress, which includes a detailed agenda for critical research needs in both life and physical sciences for future space exploration. The NRC places heavy emphasis on reduced-gravity two-phase flow and heat transfer, including the need for databases, correlations, theoretical models, and computational tools.

1.2. Microgravity testing platforms

Microgravity can be simulated in a number of platforms. An above ground *drop tower* or below ground *drop shaft* consist of a long, vertical conduit within which an experiment package is dropped to achieve microgravity during free fall. They provide very high quality residual gravity ($<1\times10^{-4}\,g_e$) for relatively short durations between 2.2 and 10 s (2.2 s for NASA Glenn Research Center's 24-m drop tower, 5.2 s for NASA Glenn Research Center's 132-m drop shaft, 4.6 s for NASA Marshall Space Flight Center's 105 m drop tower, 4.72 s for Germany Drop Tower Bremen's (ZARM's) 110-m drop tower, and 10 s for Japan Microgravity Center's (JAMIC's) 700-m drop shaft) [21]. Because of their relatively short microgravity duration, drop towers and drop shafts are typically used for initial validation of experiments before more comprehensive experiments are carried out in long-duration microgravity onboard the International Space Station (ISS). Key drawbacks of drop towers and drop shafts are (i) limited time available to achieve steady two-phase flow or to collect sufficient data for statistical analysis without a significant number of repetitive drops (since only one set of operating conditions can tested in a single drop), and (ii) inability of experimenter to manually interact with the experimental package.

Sounding rockets are another option for microgravity tests. They are sub-orbital carriers (they do not go into orbit around the Earth) and provide 3 to 13 min of low gravity with good residual gravity control ($<1\times10^{-4}\,g_e$) [21]. Like drop tower and drop shaft experiments, they preclude manual access to the experimental package and are intended for initial validation.

The ISS provides the ultimate testing environment for microgravity two-phase flow and heat transfer, providing long duration, quasi-steady environment below $1\times10^{-4}\,g_e$ [22], operator access to the experimental package, as well as automatic and remote control capabilities. However, ISS experiments are very expensive and require many years of development and safety certification, which causes great delays in the performance of much-needed microgravity experiments.

Parabolic flight aircraft provide a cost effective means to achieving microgravity with durations of 15–30 s. Preceded and followed by durations of high gravity, the microgravity period is achieved several tens of times as the aircraft undergoes a series of parabolic maneuvers. Despite relatively lower quality of residual gravity ($+/-0.01\,g_e$), which is influenced both by pilot skill and weather related turbulence, parabolic flight experiments offer significant

advantages over drop tower and drop shafts, not only in terms of longer test duration, but also the ability to accommodate larger experiment packages, use of additional intrusive instrumentation, and ability of experimenter to interact with the test. Larger experimental packages mean larger and more realistic diameters and lengths may be used to better simulate actual TCS components. Also, while it is difficult to run multiple experiments at different operating conditions in sounding rockets, this can be easily accomplished in aircraft experiments during a series of parabolas. Clearly, parabolic flight aircraft provide an effective and affordable platform for obtaining relatively large two-phase flow and heat transfer databases in microgravity, including the ability to incorporate extensive flow visualization techniques. These are key reasons behind the reliance of the present study on parabolic flight experiments.

1.3. Predictive methods for condensation heat transfer

Condensation is encountered in numerous power generation, chemical, food, and pharmaceutical industries. Condensation in tubes takes the form of a number of flow regimes, depending on the tube length. With superheated conditions at the inlet, condensation is initiated with an upstream pure vapor flow regime. Transition to annular flow occurs once the condensate film begins to form along the inner walls of the tube surrounding a central vapor core. The film is driven mostly by the vapor shear and is influenced by gravity for low flow rates. Heat transfer in the upstream, thin portion of the film is dominated by conduction. Both the flow rate and thickness of the condensate film increase along the tube, and the film flow may turn turbulent and very wavy downstream. Further thickening of the film causes wave peaks from opposite sides of the tube to merge, causing a transition to slug flow. With a further axial increase in the liquid flow rate, bubbly flow is established when the length of the slug flow bubbles falls below the tube diameter. Eventually, all remaining vapor is converted into liquid, resulting in a pure liquid flow regime.

Modeling of condensation in tubes has been focused mostly on the annular flow regime because of the ability of this regime to deliver the highest heat transfer coefficients and its prevalence over the largest fraction of the tube length. Three different approaches have been adopted to predict the condensation heat transfer coefficient: (i) empirical and semi-empirical correlations that are limited to specific fluids, operating conditions and tube geometries [23–33], (ii) 'universal' correlations that are derived from large databases that are amassed for a large number of working fluids and broad ranges of tube diameter, mass velocity, quality and pressure [34–36], and (iii) theoretical models [37,38].

Theoretical modeling of annular flow is achieved via the control-volume method by applying mass, momentum and energy conservation to the liquid film and vapor core separately and to the combined flow, and by matching velocity, temperature, shear, heat flux and mass flux at the film interface. However, theoretical modeling is complicated by (i) a lack of understanding of the transition from laminar to turbulent film flow, (ii) interfacial waves (ripples, large waves, solitary waves), (iii) dampening of turbulence at the film interface due to surface tension, and (iv) droplet and entrainment effects.

1.4. Objectives of study

The present study constitutes the first phase of NASA's Flow Boiling and Condensation Experiment (FBCE), which is projected for deployment in the International Space Station (ISS) in 2017. This initiative is aimed at amassing comprehensive flow boiling and condensation databases in microgravity, which will serve as foundation for development of mechanistic models for both. The present study concerns the condensation portion of this long-term initiative. Discussed in this paper are findings from an experimental study of condensation in microgravity that was conducted in parabolic flight using FC-72 as working fluid. Presented is a systematic assessment of the axial variations of the condensation heat transfer coefficient relative to variations in mass velocities of FC-72 and cooling fluid (water). This paper also summarizes findings from a flow visualization study of the film interface for different operating conditions. Finally, a theoretical control-volume model is constructed for condensation in microgravity, and its predictions compared to the experimental data.

2. Experimental methods

2.1. Condensation facility

The experimental apparatus used in this study is configured to provide detailed heat transfer measurements as well as facilitate high-speed video analysis of the condensing film. Two separate condensation modules are used for this purpose. The first, condensation module CM-HT, is used for acquisition of detailed heat transfer measurements for FC-72 along a circular metallic tube that is cooled by a counterflow of water through an annulus between the tube and an external channel. This flow configuration serves as an ideal geometry for comparison with theoretical condensation models. However, a key disadvantage of CM-HT is the lack of optical access to the condensation film. Therefore, a second, condensation module CM-FV, is configured to facilitate direct viewing of the film by flowing FC-72 through the annulus in a transparent outer channel, with the water flowing in the opposite direction through the inner metallic tube.

Fig. 1(a) shows the condensation facility consists of two separate sub-loops, one for FC-72 and the other for water. The FC-72 is circulated with the aid of a magnetically driven Micropump GB gear pump, followed by a flow control valve, filter, and flow meter. Before reaching the desired condensation module (CM-HT or CM-FV), the FC-72 liquid is brought to the desired quality using two Hotwatt inline electrical pre-heaters that are connected in series. The FC-72 is routed to the desired condensation module with the aid of two three-way valves. The two-phase FC-72 mixture exiting the test module is passed through a Lytron liquid-to-air heat exchanger to return the mixture to liquid state. The FC-72 sub-loop is fitted with a Flexicraft accumulator to set operating pressure. The accumulator contains metallic bellows to help accommodate any FC-72 contraction or expansion, with the chamber surrounding the bellows charged with nitrogen gas to a preset pressure.

The primary purpose of the water sub-loop is to reject the heat from the FC-72 vapor in the desired test module. The water is supplied to CM-HT or CM-FV with the aid of a Lytron modular cooling system containing a pump and fan-cooled heat exchanger. The Lytron system is modified by replacing its plastic reservoir with a stainless steel reservoir, and fitted with a Flexicraft accumulator. The water flow rate is regulated with a control valve and measured by a turbine flow meter. The water exiting CM-HT or CM-FV is returned to the Lytron system to be cooled to near-ambient temperature.

As shown in Fig. 1(a), the condensation facility includes a detachable FC-72 deaeration system consisting of a FC-72 reservoir fitted with four immersion heaters and a condensation coil that is cooled by a Lytron water-cooling system. The deaeration procedure consists of simultaneously boiling the FC-72 liquid and condensing the FC-72 vapor for 30 min, while allowing any non-condensable gases to escape to the ambient. The deaeration system is detached before the condensation facility is transported to the aircraft for testing.

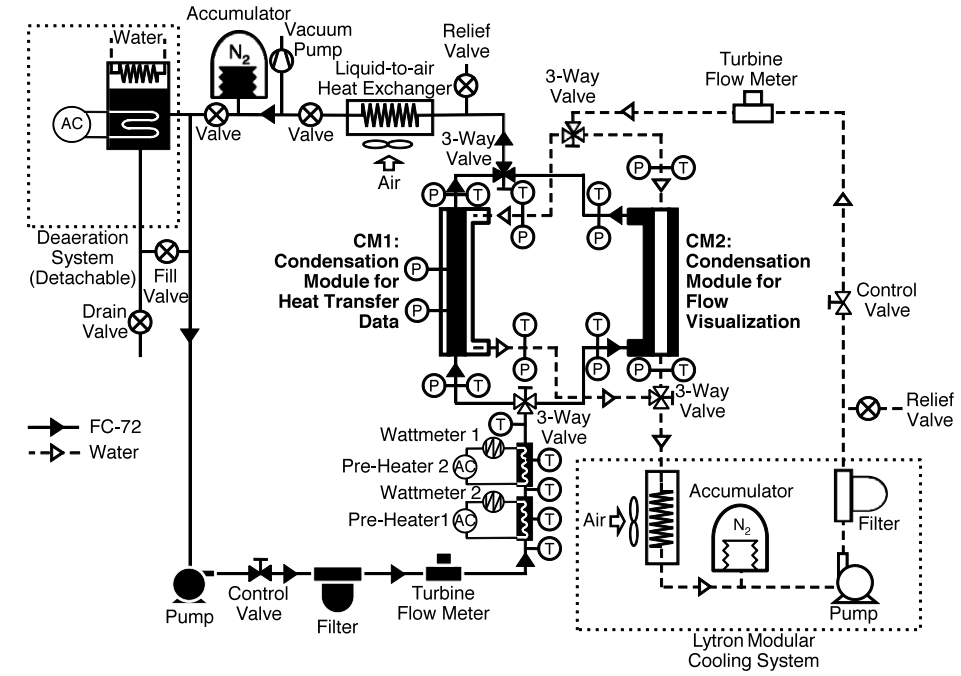

(a)

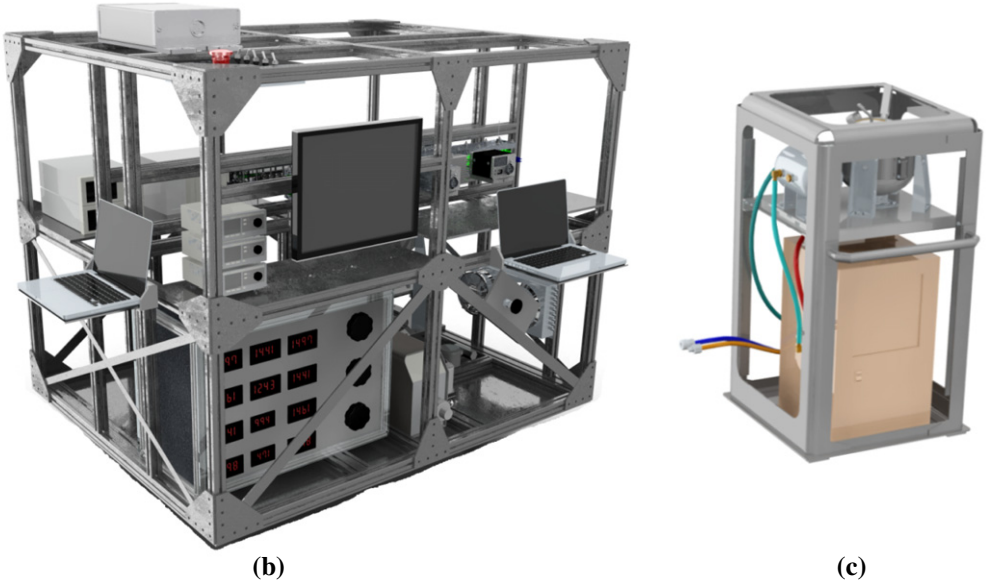

(b) (c)

Fig. 1. (a) Schematic of flow loop. (b) CAD diagram of condensation rig. (c) CAD diagram of water conditioning rig.

With the deaeration system removed, the facility consists of two parts, the main condensation rig and a water conditioning rig. Shown in Fig. 1(b), the condensation rig contains all components of the FC-72 sub-loop, the two condensation modules, and all controls, video cameras, lighting and data acquisition equipment. Components of the condensation rig are assembled into a rectangular aluminum rack that is fastened directly to the aircraft floor. The layout of components is optimized to facilitate convenient frontal access of the lead operator to a data acquisition laptop, pre-heater power controls, FC-72 control valve, pump controller, and all pressure and flow rate display panels. A second laptop is used by the lead operator to view operating conditions from the data acquisition laptop. Up to three cameras, each employing a dedicated laptop, are used to view the inlet, middle and outlet regions of CM-FV. The cameras are triggered simultaneously by the data acquisition laptop during the μg_e periods.

Fig. 1(c) shows the water conditioning rig, which contains the water pump, heat exchanger, filter, stainless steel reservoir and water accumulator. This rig is connected to the condensation rig with flexible hoses fitted with quick disconnect couplers.

2.2. Heat transfer module CM-HT

Condensation module CM-HT features FC-72 vapor flow through a central 304 stainless steel tube, and water flow in the opposite direction through an annulus as shown in Fig. 2(a). The stainless steel tube has a 7.12-mm i.d. and 0.41-mm wall thickness, and the diameter of the annulus is 12.70 mm. As shown in Fig. 2(b),

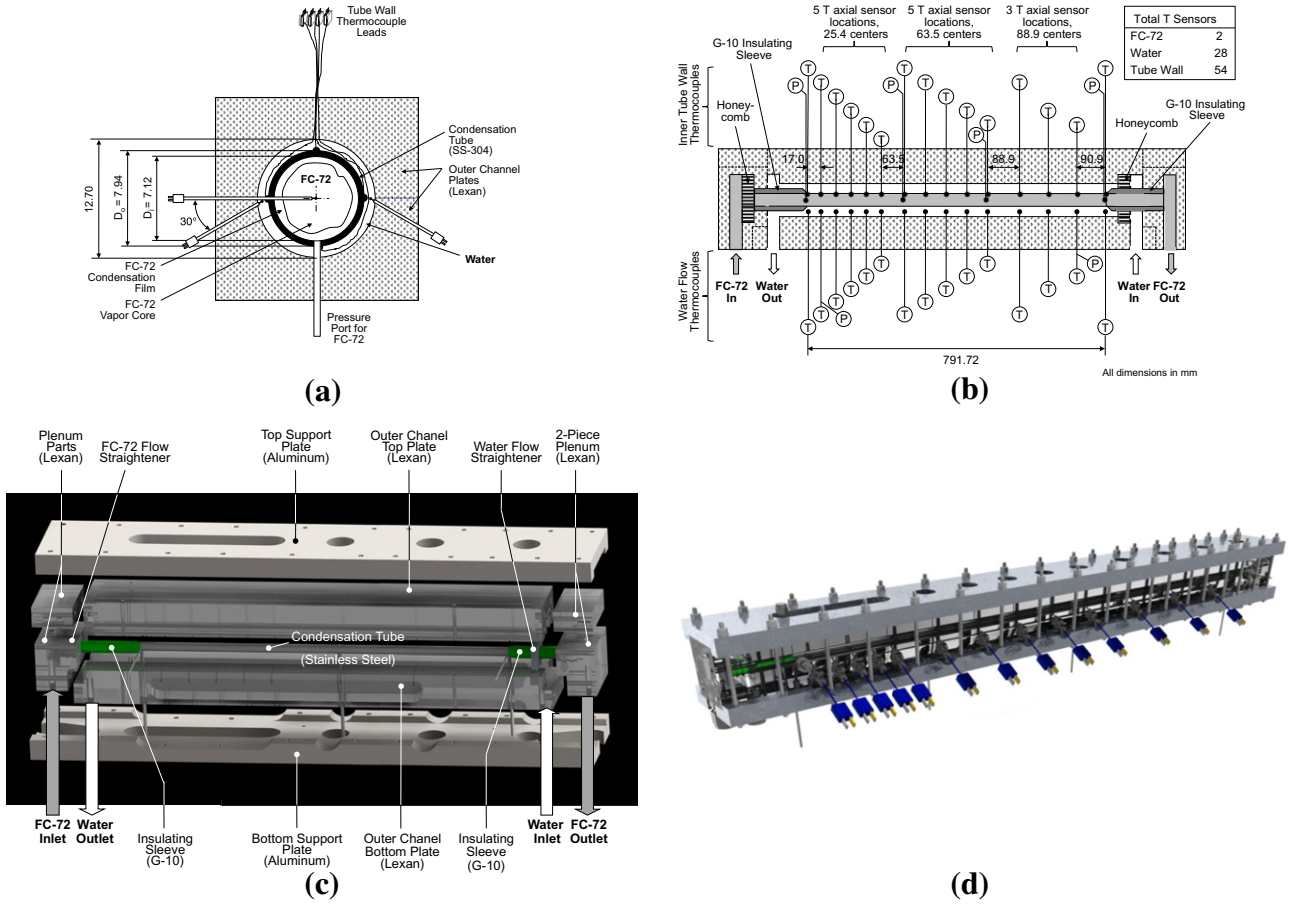

Fig. 2. Construction of condensation module CM-HT for heat transfer measurements: (a) cross-sectional diagram, (b) longitudinal sectional diagram, (c) CAD model of module parts, and (d) CAD model of module assembly with instrumentation.

the FC-72 is introduced from the left inlet and the water from the right. The left FC-72 header is fitted with an aluminum honeycomb flow straightener to ensure uniform vapor flow. A similar honeycomb flow straightener is inserted into the right water header. The central stainless steel tube is fitted on both ends with 11.1-mm o.d. low conductivity fiberglass plastic (G-10) sleeves to minimize heat transfer between the FC-72 and water upstream and downstream of the condensation length. The left sleeve defines the upstream edge for the condensing portion of the stainless steel tube, as well as ensures hydrodynamically fully developed flow at the same location. The sleeves possess a mild 6.8-degree taper at both ends of the condensing length to minimize any wake effects. The condensing length between the G-10 sleeves is 791.72 mm and the total tube length 909.83 mm.

The materials used in the construction of CM-HT are carefully selected to enhance the accuracy of the heat transfer measurements. The low thermal conductivity of the inner stainless steel tube helps minimize axial conduction in favor of radial heat transfer between the two fluids. Axial conduction is also minimized by the tube's small wall thickness. Small wall thickness also serves the purpose of expediting thermal response during μg_e periods. The outer channel of CM-HT is constructed from thermally insulating polycarbonate plastic (Lexan) to minimize heat loss to the ambient.

CM-HT is instrumented with an array of temperature and pressure sensors as illustrated in Fig. 2(a) and (b). The temperatures are measured by 36-gauge type-T thermocouples that are distributed both circumferentially and axially. There are 15 axial thermocouple stations for measurement of both stainless tube wall temperature and water temperature. Limited access reduced the number of thermocouples actually installed at these axial stations. Up to four thermocouples are installed at each of the 15 thermocouple stations to measure the stainless steel tube's wall temperature; a total of 39 thermocouples are actually used. These thermocouples as spaced 90° apart to check for circumferential symmetry of the wall temperature. There are 22 additional pairs of thermocouples installed at the same 15 axial thermocouple stations to measure the axial temperature distribution for water. These thermocouples are installed at 90- and 270-degree orientations to check for circumferential symmetry in the water temperature. Fig. 2(b) shows the axial pitch of the thermocouple stations is smaller towards the left FC-72 inlet, which is intended to capture the relatively sharp variation in the condensation heat transfer coefficient near the FC-72 inlet where the annular condensing film is thinnest. The thermocouple wires at each of the 15 axial stations are routed through a single hole in the outer channel's top Lexan plate. Because of incompatibility of the thermocouple wire insulation with sealants, the insulation is removed along the length of the hole to seal the metal wires in epoxy.

Pressures in CM-HT are measured using Honeywell STJE absolute pressure transducers at four axial locations for FC-72 and two locations for water.

Fig. 2(c) shows CM-HT consists of the inner stainless steel tube, two G-10 sleeves, two flow straighteners, and polycarbonate plastic (Lexan) parts. There are six polycarbonate parts: outer channel top and bottom plates, two blocks comprising the FC-72 inlet header, and two blocks the water inlet header. The top and bottom plates are sandwiched between two thick aluminum plates to help

prevent fluid leaks and minimize warping of the assembly. Fig. 2(d) shows CM-HT fully assembled and instrumented.

2.3. Flow visualization module CM-FV

As mentioned earlier, the major difference in the construction of CM-HT versus CM-FV is passing the FC-72 through the annulus and water the inner stainless steel tube for the latter. As shown in Fig. 3(a), the inner tube in CM-FV has a 5.99-mm o.d. and wall thickness of 0.254 mm, and the square annular region is 12.2-mm wide. Using flat rather than circular walls for the outer transparent channel provides undistorted optical access to the FC-72 film. CM-FV features both an inlet honeycomb flow straightener and inlet G-10 sleeve. Fig. 3(b) shows the temperatures and pressures are measured at the inlet and outlet for each fluid stream. Also shown is a G-10 sleeve at the FC-72 inlet, leaving a condensation length of 777.24 mm.

As shown in Fig. 3(c), CM-FV is comprised of the inner stainless steel tube, upper and lower outer channel polycarbonate plastic plates, two end header blocks, and two stainless steel support plates. Fig. 3(d) shows CM-FV fully assembled and instrumented.

2.4. Photographic methods

Three different cameras are used to capture images of the FC-72 condensate film in the inlet, middle and outlet of the condensation length in CM-FV. The inlet and middle are captured with high-speed Phantom 5 and Photron cameras, respectively, at 4000 frames per second (fps). During each parabola, the Phantom 5 camera captures a 1-s video record with 512 × 256-pixel resolution, and the Photron camera a 0.75-s record with 1024 × 128-pixel resolution. Lighting for the two cameras is provided by four green LED light sources. The outlet is captured during the entire flight period by a Pulnix CCD camera at 29.97 fps with 640 × 480-pixel resolution.

2.5. Operating conditions and measurement uncertainties

The reduced gravity environment is achieved onboard Zero-G Corporation's modified Boeing 727 jet. A μg_e period lasting approximately 17 s is achieved repeatedly during a series of parabolic maneuvers. The operating conditions for the μg_e period are set during the preceding aircraft pull-up. Five operators are required during the flight experiments.

The operating conditions for the study are as follows: FC-72 mass velocity of $G = 129.0 - 340.5$ kg/m^2 s, FC-72 inlet pressure of $P_{FC,in} = 113.7 - 126.3$ kPa (16.5–18.3 psia), FC-72 saturation temperature of $T_{sat} = 60.0 - 63.4$ °C, FC-72 inlet thermodynamic equilibrium quality of $x_{e,in}$ up to 0.98, water mass velocity of $G_w = 86.7 - 321.4$ kg/m^2 s, water inlet pressure of $P_{w,in} = 120.0 - 127.0$ kPa (17.4–18.4 psia), and water inlet temperature of $T_{w,in} = 24.4 - 27.4$ °C. The highest FC-72 film Reynolds number achieved is $Re_{film} = 3096.3$. Table 1 provides a summary of the thermophysical properties of FC-72 at $T_{sat} = 62$ °C. Notice that the inlet quality is maintained close to but below unity to prevent overheating in the second pre-heater.

Pressures throughout the condensation facility are measured by Honeywell STJE absolute pressure transducers with an accuracy of

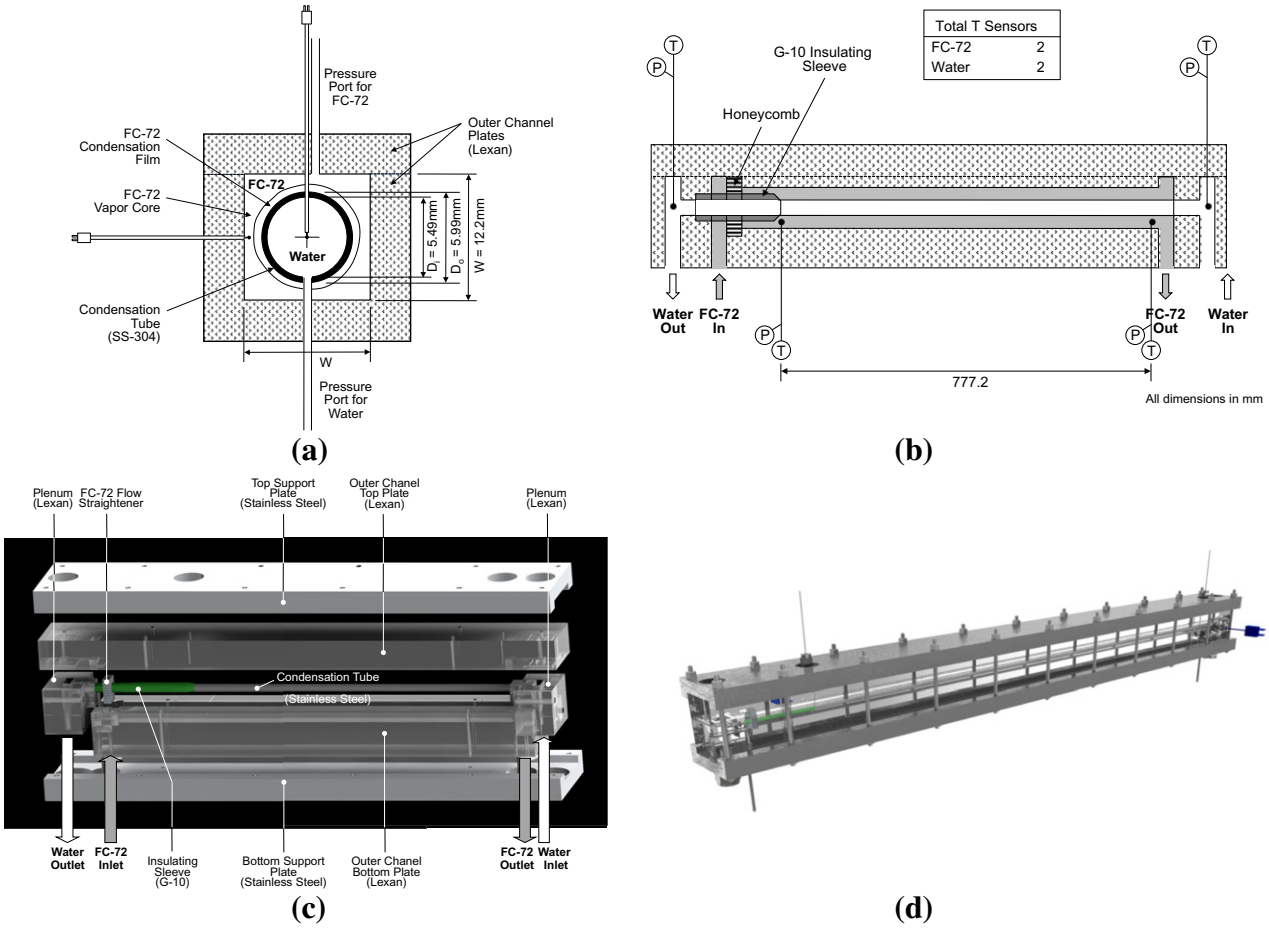

Fig. 3. Construction of condensation module CM-FV for flow visualization: (a) cross-sectional diagram, (b) longitudinal sectional diagram, (c) CAD model of module parts, and (d) CAD model of module assembly with instrumentation.

±0.05%. The temperatures are measured with type-T thermocouples having an uncertainty of ±0.4 °C. The Flow Technology Omniflo turbine flow meters used to measure the flow rates of FC-72 and water possess accuracies of ±0.25%. The accuracies of the Yokogawa WT200 and WT210 power meters used to measure the electrical power input to the first and second pre-heaters, respectively, are ±0.2% and ±0.1%. The overall uncertainty in determining the condensation heat transfer coefficient is ±8.88%.

3. Flow visualization results

Fig. 4(a) shows sequential images of the FC-72 condensation film along the outer surface of the stainless steel tube inside CM-FV for FC-72 mass velocities of G = 38.0, 63.8 and 128.8 kg/m^2 s at water mass velocities in a narrow range of G_w = 248.5 – 272.8 kg/m^2 s. Each image is 40-mm long and centered at z = 5.8 cm from the inlet of the condensation length. These images

Table 1
Thermophysical properties of saturated FC-72 at 62 °C (P = 1.21 bar).

k_f [W/m K]	μ_f [kg/m s]	$c_{p,f}$ [J/kg K]	σ [mN/m]	h_f [kJ/kg]	h_{fg} [kJ/kg]	ρ_f [kg/m^3]	ρ_g [kg/m^3]
0.0532	409×10^{-6}	1110	7.8	101.93	93.03	1578	15.86

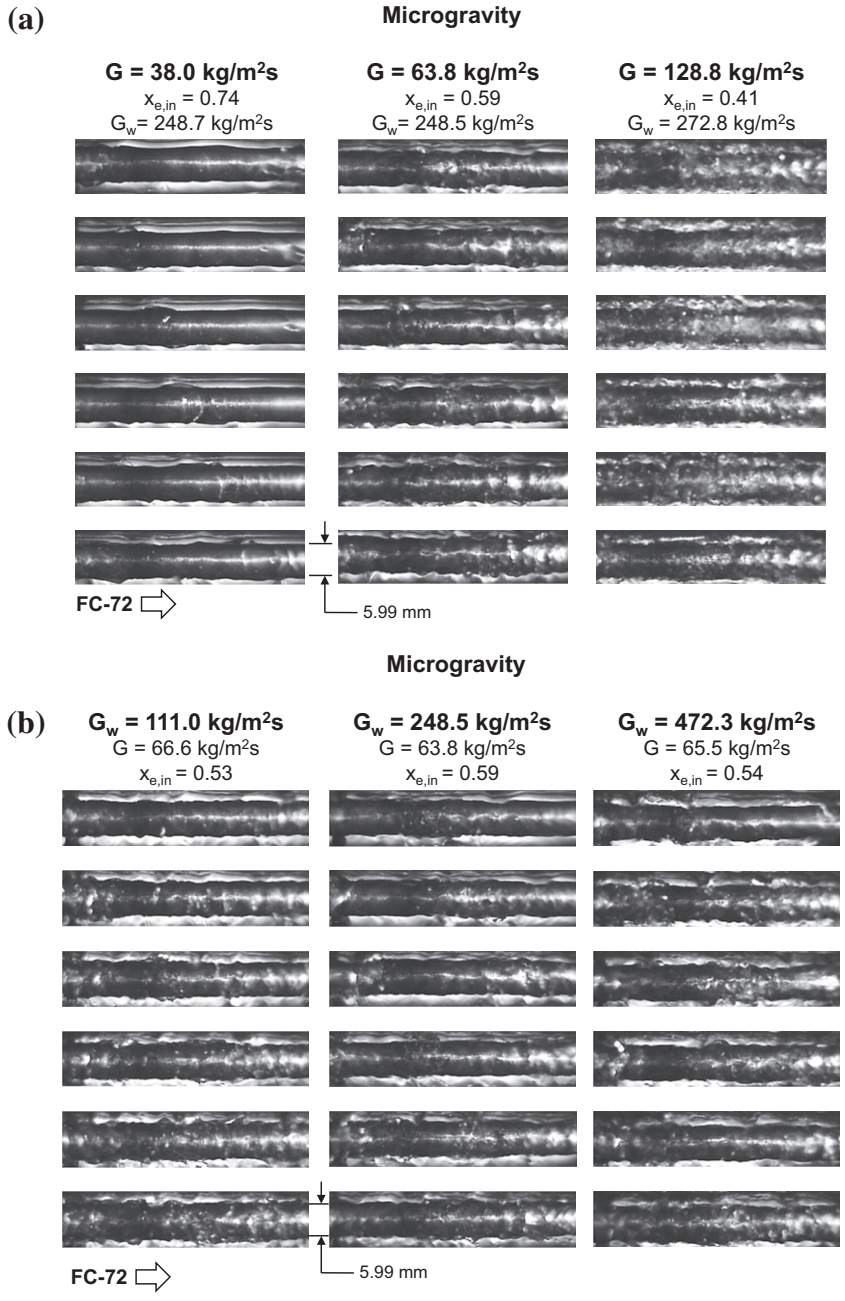

Fig. 4. Sequential images of condensation film along outer surface of central stainless steel tube of CM-FV in microgravity for (a) three FC-72 mass velocity and nearly constant water mass velocity, and (b) three water velocities and nearly constant FC-72 mass velocity, with individual images in each sequence separated by 0.03 s. The images are centered at z = 5.8 cm from inlet of condensation length.

were captured by the high-speed Phantom 5 video camera at 4000 fps. At $G = 38.0$ kg/m^2 s, the FC-72 film appears laminar and the interface fairly smooth between widely separated wave peaks region. At $G = 63.8$ kg/m^2 s, the film appears laminar but quite wavy. The flow turns turbulent at $G = 128.8$ kg/m^2 s, marred by both small ripples and fast moving large waves.

Fig. 4(b) shows sequential images of the condensation film for water mass velocities of $G_w = 111.0$, 248.5 and 472.3 kg/m^2 s, and FC-72 mass velocities in a narrow range of $G = 63.8$–66.6 kg/m^2 s. Despite the large variations in G_w, all images in Fig. 4(b) depict a wavy-laminar interface similar to that in Fig. 4(a) for $G = 63.8$ kg/m^2 s. This shows that the film flow is far more sensitive to G than to G_w.

Fig. 5 compares video images of the condensation film in microgravity, Lunar gravity (0.17 g_e) and Martian gravity (0.377 g_e) for two sets of operating conditions. At the lower FC-72 mass velocity, the film in microgravity is predominantly smooth-laminar and increases in thickness in the flow direction due to condensation, with waves appearing towards the downstream edge of the image. For a similar FC-72 mass velocity, Lunar gravity causes the film to thicken beneath the tube while maintaining a predominantly wavy-laminar character. The underside thickening is more severe in Martian gravity, which also causes appreciable thinning on the top portion of the tube. The circumferential variations of film thickness under Lunar gravity and Martian gravity cause appreciable circumferential variations in the film's flow rate and therefore heat transfer rate.

At the higher FC-72 mass velocity, Fig. 5 shows the film is turbulent and very wavy for all three gravity levels, with the film showing no underside thickening in either Lunar gravity or Martian gravity. This behavior may be explained by the appreciable increase in vapor shear stress on the film for the high FC-72 mass velocity.

These trends point to an important practical conclusion concerning the implementation of condensation in space missions involving multiple gravity fields: it is possible to negate the influence of gravity altogether by increasing the flow rate of the working fluid.

4. Heat transfer results

4.1. Data reduction method

A differential resistance network is adopted to determine the local condensation heat transfer coefficient, $h(z)$, for condensation module CM-HT. Since the water temperature, $T_w(z)$, and outer wall temperature of the stainless steel tube, $T_{wall,o}(z)$, in CM-HT are measured at specific axial stations, continuous distributions for these temperatures are first determined from curve fits to the measured values. These curve fits are then used to determine T_w and $T_{wall,o}$ at the midpoints between axial measurement stations. Fig. 6(a) shows how these calculations are carried out between measurement stations n and $n+1$. The differential heat transfer rate, Δq, from the FC-72 to the water over axial distance Δz between the two thermocouple stations is equal to the increase in sensible heat of water over Δz, which is proportional to the water temperature rise ΔT_w measured between the two stations. Notice that the stainless steel tube's inner wall temperature, $T_{wall,i}$, is not measured but calculated by accounting for the temperature drop due to thermal resistance across the tube wall. The FC-72 condensation heat transfer coefficient, $h(z)$, at the midpoint between stations n and $n+1$ is determined from the relation

$$\Delta q = \dot{m}_w c_{p,w}, \Delta T_w = \frac{T_{wall,i} - T_{wall,o}}{\frac{\ln(D_o/D_i)}{2\pi k_{ss}\Delta z}} = h(z)(\pi D_i \Delta z)[T_{sat}(z) - T_{wall,i}(z)] \quad (1)$$

which amounts to two equations with two unknowns, $T_{wall,i}(z)$ and $h(z)$. The quality of FC-72 at the inlet to the condensation module, $x_{e,in}$, is calculated from an energy balance to the two pre-heaters upstream of CM-HT based the mass flow rate of FC-72, measured FC-72 temperature at the inlet to the first pre-heater, and electrical power input to the two pre-heaters. The thermodynamic equilibrium quality, $x_e(z)$, at the midpoint between stations n and $n+1$ is obtained by accounting for all the heat transferred from the FC-72 to the water between 0 and z.

$$x_e(z) = x_{e,in} - \frac{\sum_{j=1}^{n}\Delta q_j + \frac{\Delta q_{n+1}}{2}}{h_{fg}}. \quad (2)$$

The FC-72 properties in Eqs. (1) and (2) are nearly constant because pressure drop along the condensation length is quite small (<2.93 kPa). These properties are calculated at saturation temperature, T_{sat}, of FC-72 based on the average of measured inlet and outlet pressures.

4.2. Steady-state conditions

Fig. 6(b) shows temporal records of the heat transfer coefficient at four axial locations along the condensation tube corresponding

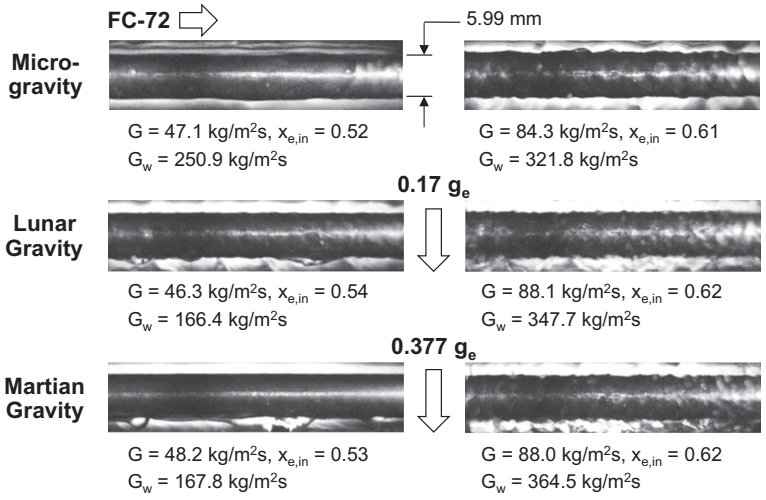

Fig. 5. Comparison of images of condensation film in microgravity, Lunar gravity and Martian gravity for two sets of operating conditions. The images are centered at $z = 5.8$ cm from inlet of condensation length.

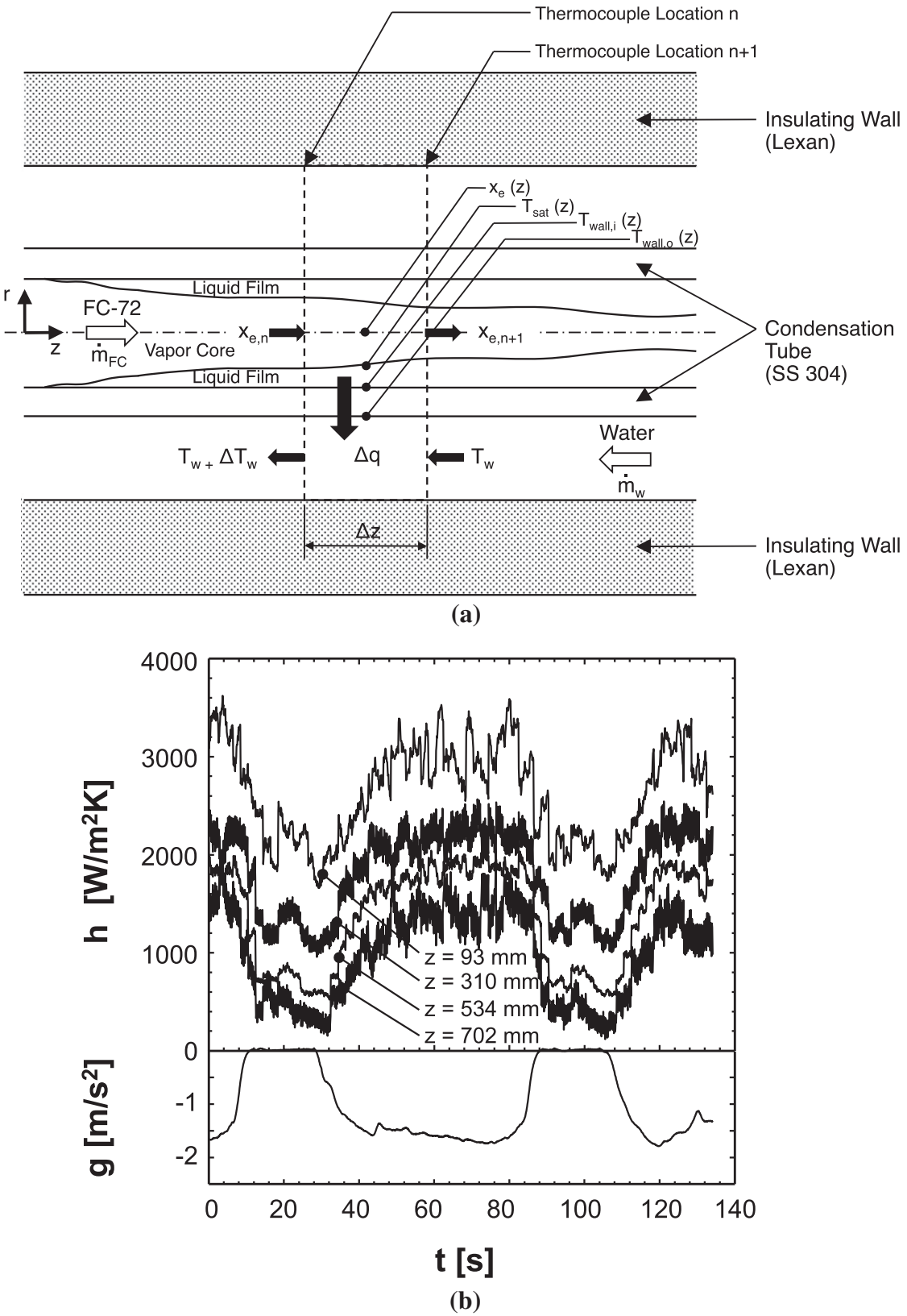

Fig. 6. (a) Thermal model used to determine the axial variations of water temperature, outer wall temperature, and FC-72 quality, x_e. (b) Variation of condensation heat transfer at four axial locations during gravity changes corresponding to two microgravity parabolas for $G = 264.1$ kg/m^2 s, $G_w = 186.9$ kg/m^2 s, and $x_{e,in} = 0.73$.

to two consecutive parabolas. Also shown is the corresponding temporal record of gravity. Each parabola is initiated with a 60-s, 1.8-g_e (hyper-g_e) 'pull-up', followed by approximately 17 s of μg_e, and terminated with a 1.8-g_e (hyper-g_e) 'pullout' before initiating a pull-up for the next parabola. The pullout plus pull-up duration between consecutive μg_e periods is about 40 s. A typical day of

testing consists of a two-hour flight comprised of 40 parabolic maneuvers, with each parabola lasting about 17 s, and every 10 parabolas separated by a 5-min aircraft turnaround break.

The data presented in the present study are for condensation during the microgravity periods. Notice in Fig. 6(b) how the heat transfer coefficient decreases during mg_e and increases during the pull-up and the pull-out. Because of the short duration of microgravity (~17 s) during a parabola, there is obvious concern over the ability to reach steady state and yield meaningful microgravity data. Therefore, several measures were adopted to reduce the thermal response time of the condensation facility. The response time is a complicated function of thermal mass of the test module and flow loop, fluid inventory, and operating conditions. In fact, initial flight experiments did show that data for certain operating conditions were susceptible to appreciable oscillation and could not reach steady state. Further ground tests showed that, when changing operating conditions, the response time could be significantly reduced if conditions in the FC-72 sub-loop, especially the FC-72 mass velocity, are maintained constant, while the water flow rate is increased. One reason for the small response time associated with increasing the water flow rate is the small water inventory used.

Fig. 7(a)–(c) show temporal records of the variations of outer condensation tube wall temperature, T_{wall}, water temperature, T_w, and condensation heat transfer coefficient, h, along the condensation length during the microgravity period of a single parabola. The wall temperature, Fig. 7(a), and water temperature, Fig. 7(b), show little temporal change because operating conditions are set at the beginning of the pull-up. However, Fig. 7(c) shows an appreciable temporal drop in h at $t = 0$, especially near $z = 0$, and steady-state conditions are achieved in the last 3–4 s of the microgravity period.

Careful assessment of the microgravity data showed that about a third of the tests could not reach steady state; data for these test were therefore discarded. In the following, only tests that yielded steady state conditions are used for analysis of the condensation heat transfer coefficient. For these tests, the condensation heat transfer coefficient is based on steady state data measured during the last 1–2 s of the microgravity period.

4.3. Assessment of circumferential symmetry of heat transfer coefficient

As shown in Fig. 2(a), the outer wall temperature of the stainless steel tube in CM-HT is measured at 15 axial stations along the condensation length, with up to 4 thermocouples per station positioned circumferentially in 90-degree angle increments. Fig. 8(a) and (b) show, for two sets of operating conditions, the variation of the condensation heat transfer coefficient along the condensation length calculated from measurements by the four individual thermocouples, along with the heat transfer coefficient based on the average of the four temperatures. Good agreement between results based on the individual thermocouples proves the film condensation is symmetrically very uniform. This is consistent with the video records depicted in Figs. 4(a), (b) and 5 which show symmetrical film thickness around the condensation tube in CM-FV for all microgravity conditions. It should be mentioned that all subsequent heat transfer coefficient results discussed in this paper are based on the average of the four thermocouple measurements.

4.4. Parametric trends of condensation heat transfer coefficient

Using CM-HT, the experimental data are used to determine the local condensation heat transfer coefficient, $h(z)$, for different combinations of FC-72 and water mass velocities within a very narrow range of FC-72 inlet qualities. Fig. 9(a)–(c) show the axial variations of h for three narrow ranges of water mass velocity. Each figure captures the influence of FC-72 mass velocity, G, on $h(z)$ for a

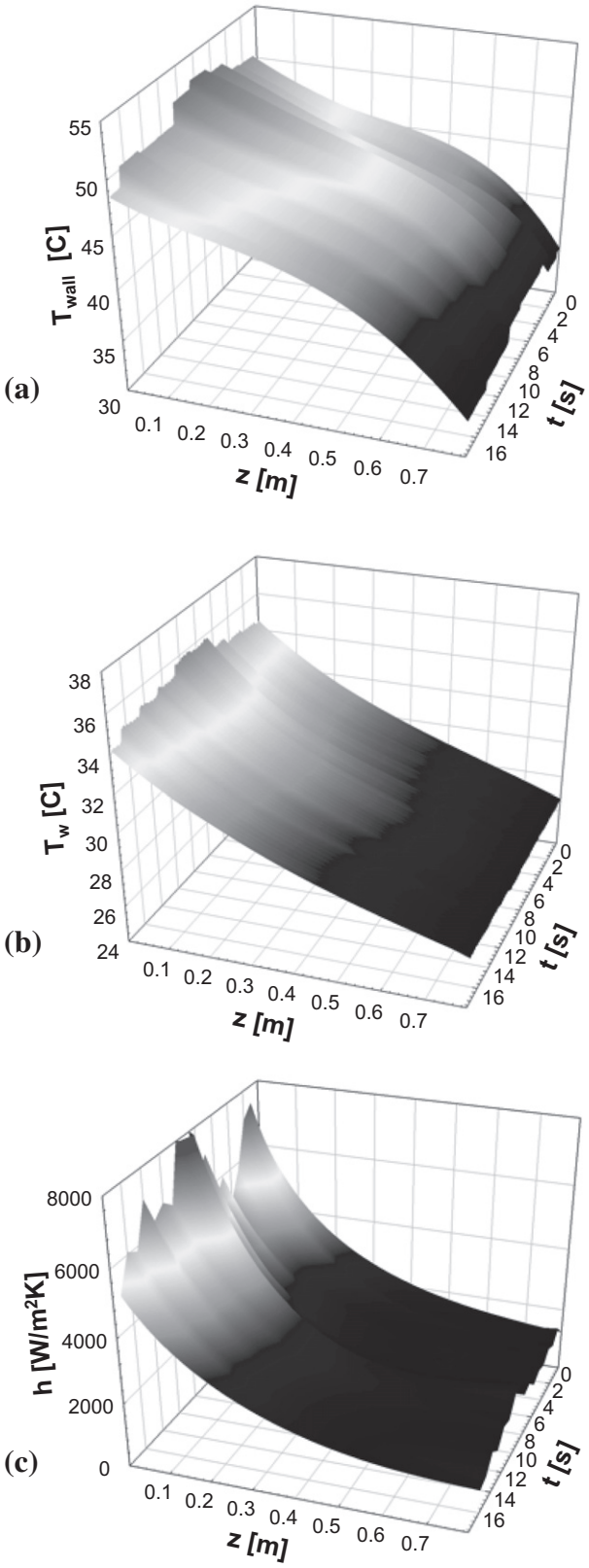

Fig. 7. Variations of (a) outside tube wall temperature, (b) water temperature, and (c) condensation heat transfer coefficient with axial distance and time during microgravity period for $G = 264.1$ kg/m^2 s, $x_{e,in} = 0.73$ and $G_w = 186.9$ kg/m^2 s.

fairly constant water mass velocity, G_w. Fig. 9(a) shows $h(z)$ for four FC-72 mass velocities of G = 144.6, 268.3, 270.1 and 329.3 kg/m^2 s at water mass velocities in a narrow range of G_w = 161.8 – 174.4 kg/m^2 s. For each FC-72 mass velocity, h is highest near the inlet and decreases along the condensation length. This trend is attributed to the condensation film being thinnest near the inlet and increasing in thickness along the condensation length. Furthermore, heat transfer within the thin upstream laminar region of the film is dominated by conduction resistance across the film, which increases with z. This trend is monotonic for the three lowest G values. However, the highest FC-72 mass velocity of G = 329.3 kg/m^2 s produces a minimum followed by a downstream increase in $h(z)$. This behavior can be explained by a downstream enhancement in heat transfer due to the film turning turbulent and to increased interfacial waviness. Fig. 9(a) also shows h generally increases with increasing G, which is the result of the film thinning achieved by higher vapor shear. Fig. 9(b) and (c) show similar trends of decreasing h with z and better heat transfer with increasing G.

Fig. 10(a)–(f) show variations of $h(z)$ for six narrow ranges of G. These figures show h mostly decreasing monotonically along the condensation length. However, the influence of G_w in Fig. 10(a)–(f) is significantly weaker than that of G in Fig. 9(a)–(c). These trends demonstrate a far stronger dependence of h on G than on G_w.

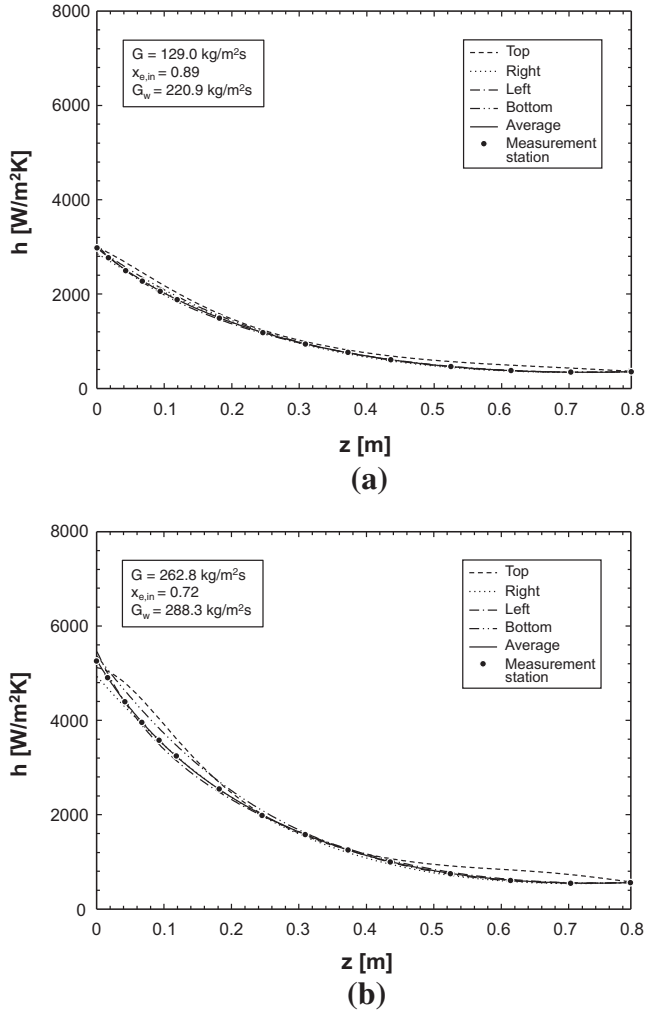

Fig. 8. Variations of experimentally-determined condensation heat transfer coefficient with axial distance as measured by four circumferential thermocouples for (a) G = 129.0 kg/m^2 s, G_w = 220.9 kg/m^2 s and $x_{e,in}$ = 0.89, and (c) G = 262.8 kg/m^2 s, G_w = 288.3 kg/m^2 s and $x_{e,in}$ = 0.72.

5. Microgravity condensation model

5.1. Model assumptions and formulation

The model presented here is based on the control volume method, which has been proven very successful at predicting heat transfer in a variety of separated two-phase flows [39–42]. Recently, Kim and Mudawar [37] adopted the control volume method to develop a model for annular flow condensation in small channels. They also provided experimental evidence that entrainment and

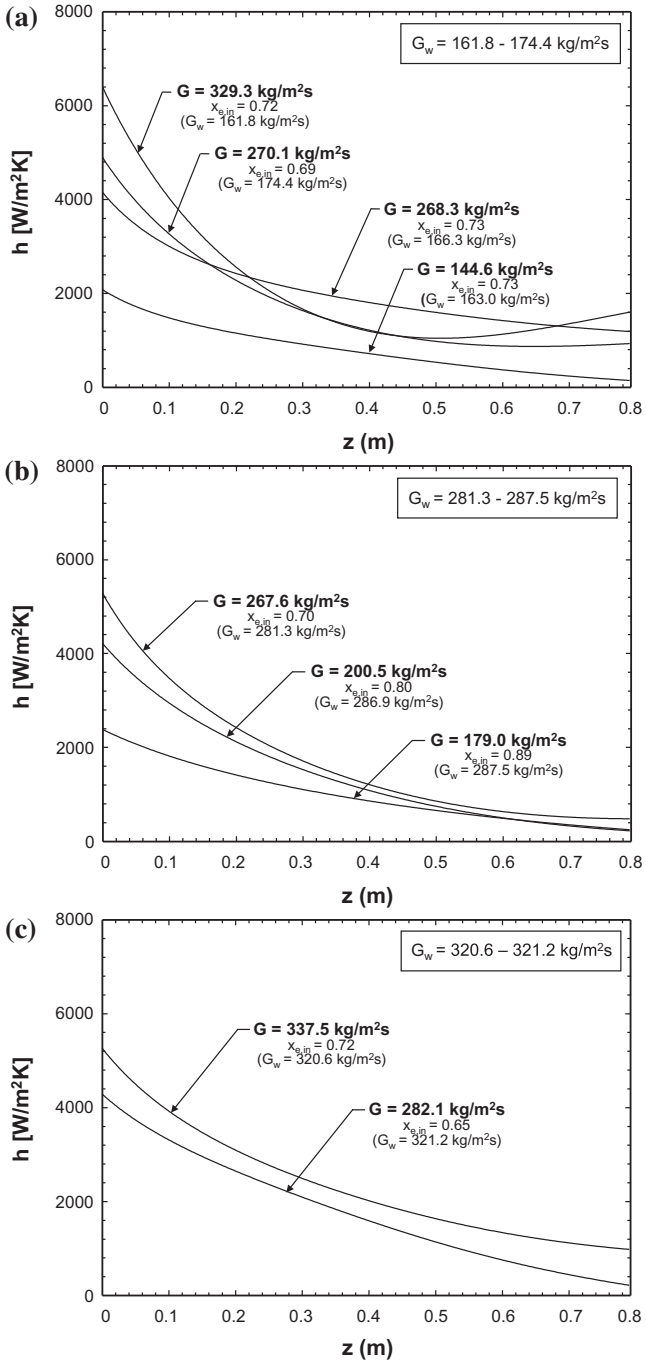

Fig. 9. Variations of experimentally-determined condensation heat transfer coefficient with axial distance for different FC-72 mass velocities and water mass velocities of (a) G_w = 161.8 – 174.4 kg/m^2 s, (b) G_w = 281.3 – 287.5 kg/m^2 s and (c) G_w = 320.6 – 321.2 kg/m^2 s.

deposition effects that are prevalent in annular flow boiling are nonexistent in annular condensing flows.

The microgravity model employed here is based on the formulations of Kim and Mudawar [37] and Park et al. [38]. The model assumes that the flow is annular and steady, and pressure is uniform across the flow area. As verified experimentally, both the film thickness and heat transfer coefficient are assumed circumferentially uniform. Furthermore, the condensing fluid is assumed to enter the condensing tube as a two-phase mixture with a quality $x_{e,in}$ smaller than but close to unity, such that a liquid film with finite thickness is available at the inlet. All thermodynamic properties of liquid and vapor are based on local saturation pressure, which is allowed to vary along the tube. Table 2 summarizes the model's key relations.

5.2. Mass conservation

The model development is initiated by discretizing the condensation length into small axial elements of length Δz, and applying mass, momentum and energy conservation to control volumes encompassing the annular film and vapor core. The total FC-72 mass flow rate, $\dot{m}$, is the sum of flow rates of the liquid film, $\dot{m}_y$ and vapor core, $\dot{m}_g$. Relations for $\dot{m}_f$, $\dot{m}_g$, and the interfacial mass

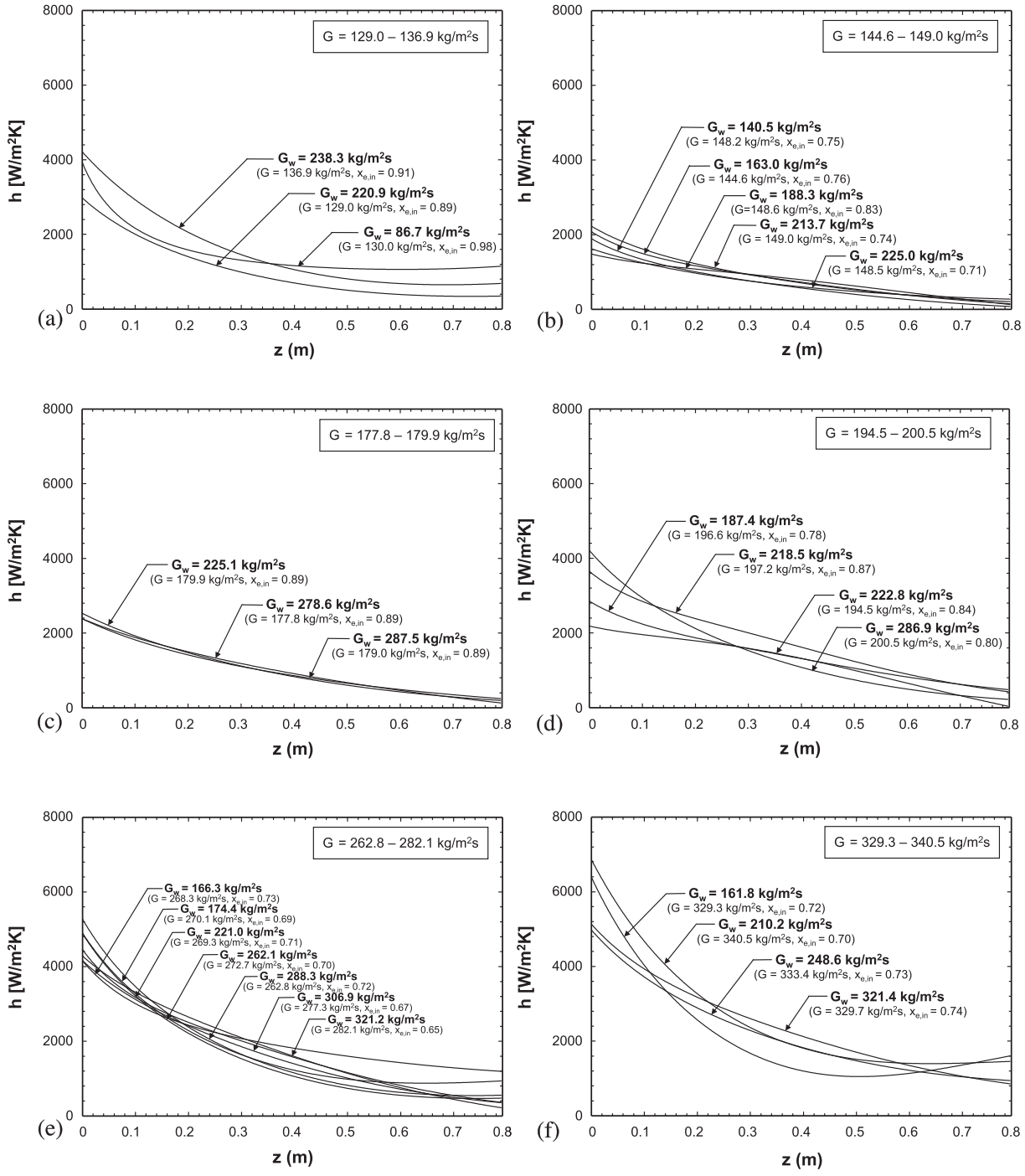

Fig. 10. Variations of experimentally-determined condensation heat transfer coefficient with axial distance for different water mass velocities and FC-72 mass velocities of (a) G = 129.0 – 136.9 kg/m^2 s, (b) G = 144.6 – 149.0 kg/m^2 s, (c) G = 177.8 – 179.9 kg/m^2 s, (d) G = 194.5 – 200.5 kg/m^2 s, (e) G = 262.8 – 282.1 kg/m^2 s, and (f) G = 329.3 – 340.5 kg/m^2 s.

Table 2
Summary of mass and momentum conservation relations of condensation model.

Mass conservation
Inlet mass flow rates of liquid film and vapor core:
$\dot{m}_{f,in} = (1 - x_{e,in})\dot{m}, \dot{m}_{g,in} = x_{e,in}\dot{m}$
Mass flow rates of liquid film and vapor core:
$\dot{m} = \dot{m}_f + \dot{m}_g$
$\dot{m}_f = \rho_f \int_0^{\delta} u_f \pi(D_i - 2y)dy = (1 - x_e)\dot{m}$
$\dot{m}_g = \rho_g \bar{u}_g \pi(D_i - 2\delta)^2/4 = x_e\dot{m}$
Mass transfer rate between liquid film and vapor core:
$\frac{d\dot{m}_f}{dz} = -\frac{d\dot{m}_g}{dz} = \Gamma_{fg}$,
where $\Gamma_{fg} = \frac{q''_w \pi D_i}{h_{fg}}$
Momentum conservation
(a) Momentum conservation for liquid film, Fig. 11(a):
Liquid film shear stress:
$\tau = \left(-\frac{dp}{dz}\right)\frac{A_{f,*}}{P_{f,y}} + \frac{\tau_i P_{f,\delta} + \Gamma_{fg} u_i}{P_{f,y}} = \mu_f\left(1 + \frac{\varepsilon_m}{\nu_f}\right)\frac{du_f}{dy}$
where $A_{f,*} = \frac{\pi}{4}(D_i - 2y)^2 - \frac{\pi}{4}(D_i - 2\delta)^2, P_{f,y} = \pi(D_i - 2y), P_{f,\delta} = \pi(D_i - 2\delta)$
Liquid film velocity profile:
$u_f(y) = \left(-\frac{dp}{dz}\right)\frac{\delta}{\mu_f}\int_0^{y/\delta}\frac{A_{f,*}}{P_{f,y}}\left(1 + \frac{\varepsilon_m}{\nu_f}\right)^{-1} d\left(\frac{y}{\delta}\right) + \frac{\delta}{\mu_f}(\tau_i P_{f,\delta} + \Gamma_{fg} u_i)\int_0^{y/\delta}\frac{1}{P_{f,y}}\left(1 + \frac{\varepsilon_m}{\nu_f}\right)^{-1} d\left(\frac{y}{\delta}\right)$
Liquid film's interfacial velocity:
$u_i = \frac{\left(-\frac{dp}{dz}\right)\frac{\delta}{\mu_f}\int_0^1 \frac{A_{f,*}}{P_{f,y}}\left(1 + \frac{\varepsilon_m}{\nu_f}\right)^{-1} d\left(\frac{y}{\delta}\right) + \frac{\delta}{\mu_f}(\tau_i P_{f,\delta})\int_0^1 \frac{1}{P_{f,y}}\left(1 + \frac{\varepsilon_m}{\nu_f}\right)^{-1} d\left(\frac{y}{\delta}\right)}{1 - \frac{\delta}{\mu_f}(\Gamma_{fg})\int_0^1 \frac{1}{P_{f,y}}\left(1 + \frac{\varepsilon_m}{\nu_f}\right)^{-1} d\left(\frac{y}{\delta}\right)}$
Pressure gradient:
$-\frac{dP}{dz} = \frac{\frac{\mu_f \dot{m}_f}{\rho_f \delta^2} - (\tau_i P_{f,\delta} + \Gamma_{fg} u_i)\int_0^1 \left[P_{f,y}\int_0^{y/\delta}\frac{1}{P_{f,y}}(1 + \frac{\varepsilon_m}{\nu_f})^{-1} d\left(\frac{y}{\delta}\right)\right] d\left(\frac{y}{\delta}\right)}{\int_0^1 \left[P_{f,y}\int_0^{y/\delta A_{f,*}}\frac{}{P_{f,y}}\left(1 + \frac{\varepsilon_m}{\nu_f}\right)^{-1} d\left(\frac{y}{\delta}\right)\right] d\left(\frac{y}{\delta}\right)}$
(b) Momentum conservation for vapor core, Fig. 11(b):
Interfacial shear stress:
$\tau_i = \frac{1}{P_{f,\delta}}\left[A_g\left(-\frac{dP}{dz}\right) - \frac{d}{dz}(\rho_g \bar{u}_g^2 A_g) - \Gamma_{fg} u_i\right]$
where $A_g = \pi(D_i - 2\delta)^2/4$
Interfacial shear stress relation (Wallis [43]):
$\tau_i = \frac{1}{2} f_i \rho_g (\bar{u}_g - u_i)^2 + \frac{(\bar{u}_g - u_i)\Gamma_{fg}}{2P_{f,\delta}}$
Interfacial friction factor (Shah and London [44]):
$f_i = 16/\mathrm{Re}_g$ for $\mathrm{Re}_g < 2000$
$f_i = 0.079\mathrm{Re}_g^{-0.25}$ for $2000 \leqslant \mathrm{Re}_g < 20,000$
$f_i = 0.046\mathrm{Re}_g^{-0.2}$ for $\mathrm{Re}_g > 20,000$,
where $\mathrm{Re}_g = \frac{\rho_g(\bar{u}_g - u_i)(D_i - 2\delta)}{\mu_g}$

transfer rate, Γ_{fg}, between the vapor core and liquid film are provide in Table 2.

5.3. Momentum conservation

Neglecting axial momentum changes of the liquid film, momentum conservation for the liquid film's control volume in Fig. 11(a) yields a relation for the shear stress in the film, τ, which is provided in Table 2. Substituting this relation with the relation for the film's mass transfer rate yields an expression for the velocity profile across the liquid film, $u_f(y)$, which is used to determine the film's interfacial velocity, u_i, by substituting $y = \delta$.

Next, the relations for $u_f(y)$ and u_i are used to derive the relation for pressure gradient across the film given in Table 2. Determining the pressure drop requires an expression for the interfacial shear stress, τ_i, which is derived by applying momentum conservation to the vapor core as shown in Fig. 11(b). The interfacial shear stress must account for both interfacial friction between the vapor core and liquid film, and interfacial mass transfer, as proposed by Wallis [43]. The present model uses the friction relations of Shah and London [44].

5.4. Determination of condensation heat transfer coefficient

The local heat flux across the liquid film is given by

$$q'' = -k_f\left[1 + \frac{\mathrm{Pr}_f}{\mathrm{Pr}_{f,T}}\frac{\varepsilon_m}{\nu_f}\right]\frac{dT}{dy} \tag{3}$$

where $\mathrm{Pr}_{f,T}$ is the turbulent Prandtl number. The local condensation heat transfer coefficient is determined by integrating Eq. (3) between the interface, where $T = T_{sat}$, and the wall, where $T = T_{wall}$,

$$h = \frac{-q''}{T_{sat} - T_{wall}} = \frac{\delta/k_f}{\left[\int_0^1 \left(1 + \frac{\mathrm{Pr}_f}{\mathrm{Pr}_{f,T}}\frac{\varepsilon_m}{\nu_f}\right)^{-1} d\left(\frac{y}{\delta}\right)\right]}. \tag{4}$$

5.5. Determination of liquid film's turbulence parameters

Two key unknowns in the condensation model's relations are the liquid film's eddy momentum diffusivity, ε_m, and turbulent Prandtl number, $\mathrm{Pr}_{f,T}$.

Using the turbulent mixing length relation originally proposed by Van Driest [45] and later modified by Kays [46], Kays and Crawford [47], Kim and Mudawar [37] proposed the following eddy diffusivity relation that is both gravity independent and accounts for interfacial dampening of turbulent fluctuations due to surface tension,

$$\frac{\varepsilon_m}{\nu_f} = -\frac{1}{2} + \frac{1}{2}\sqrt{1 + 4K^2 y^{+2}\left[1 - \exp\left(-\sqrt{\frac{\tau}{\tau_{wall}}}\frac{y^+}{A^+}\right)\right]^2 \frac{\tau}{\tau_{wall}}\left(1 - \frac{y^+}{\delta^+}\right)^{0.1}} \tag{5}$$

where $y^+ = yu^*/\nu_f, \delta^+ = \delta u^*/\nu_f, u^* = \sqrt{\tau_{wall}/\rho_f}, A^+ = 26[1 + 30.18\mu_f\rho_f^{-0.5}\tau_{wall}^{-1.5}(dP/dz)]^{-1}$, and the Von-Karman constant is given by

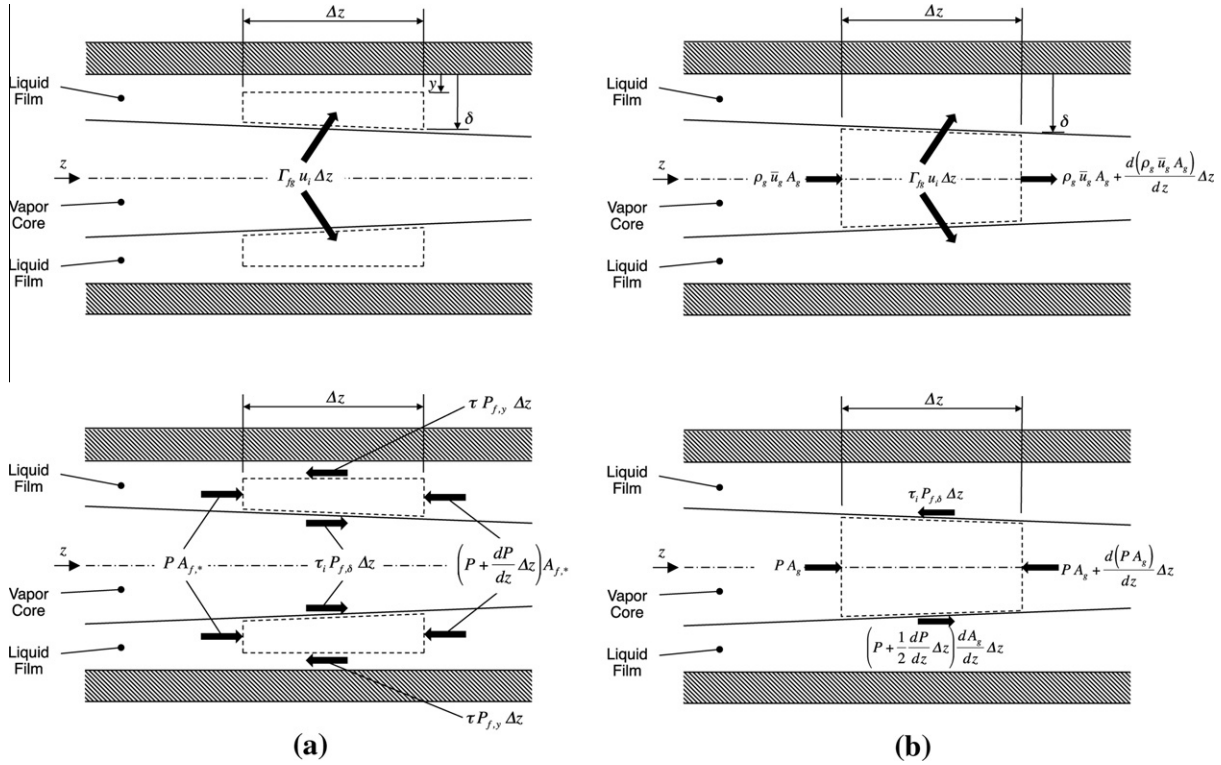

Fig. 11. Momentum and force interactions for (a) liquid film and (b) vapor core control volumes.

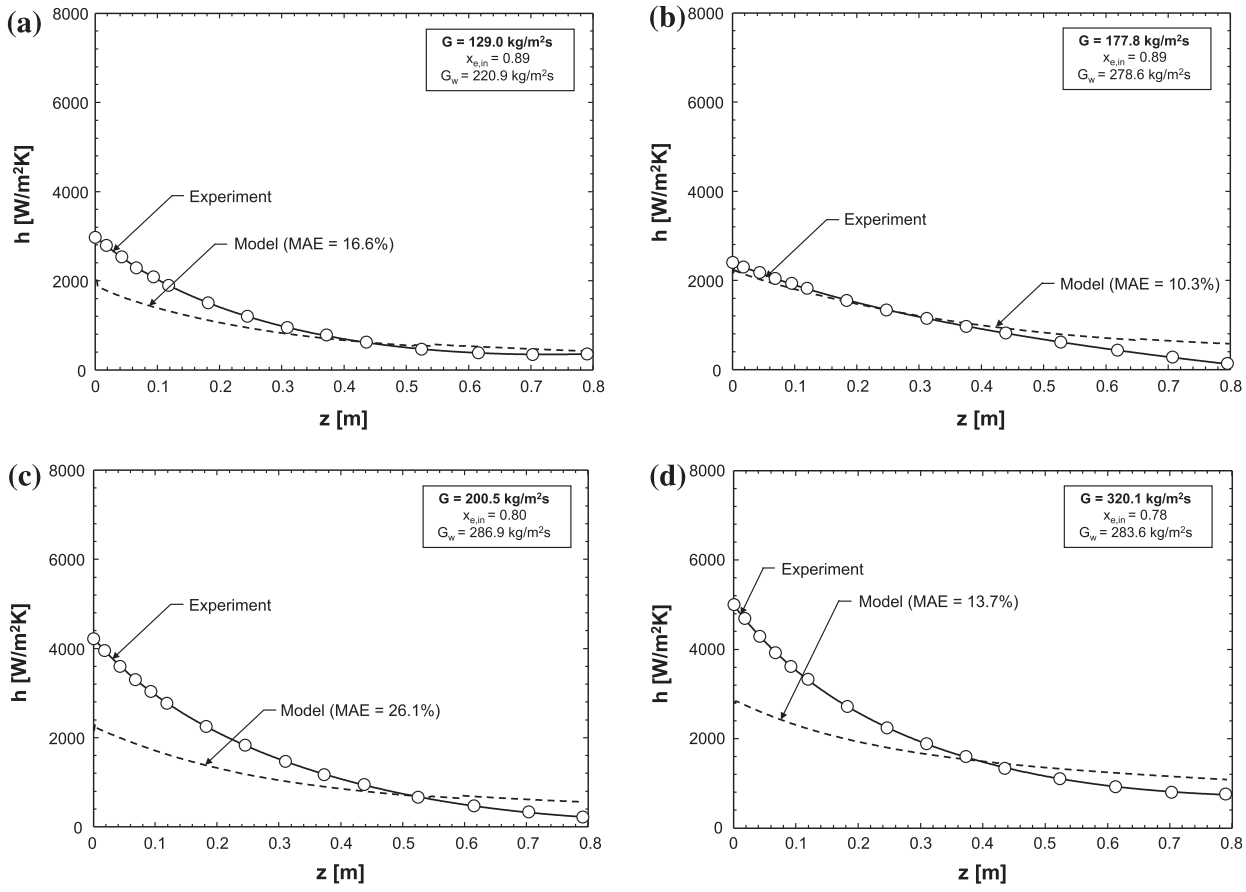

Fig. 12. Comparison of experimentally-determined axial variations of condensation heat transfer coefficient with model predictions for (a) G = 129.0 kg/m^2 s, $x_{e,in}$ = 0.89 and G_w = 220.9 kg/m^2 s, (b) G = 177.8 kg/m^2 s, $x_{e,in}$ = 0.89 and G_w = 278.6 kg/m^2 s, (c) G = 200.5 kg/m^2 s, $x_{e,in}$ = 0.80 and G_w = 286.9 kg/m^2 s, and (d) G = 320.1 kg/m^2 s, $x_{e,in}$ = 0.78 and G_w = 283.6 kg/m^2 s.

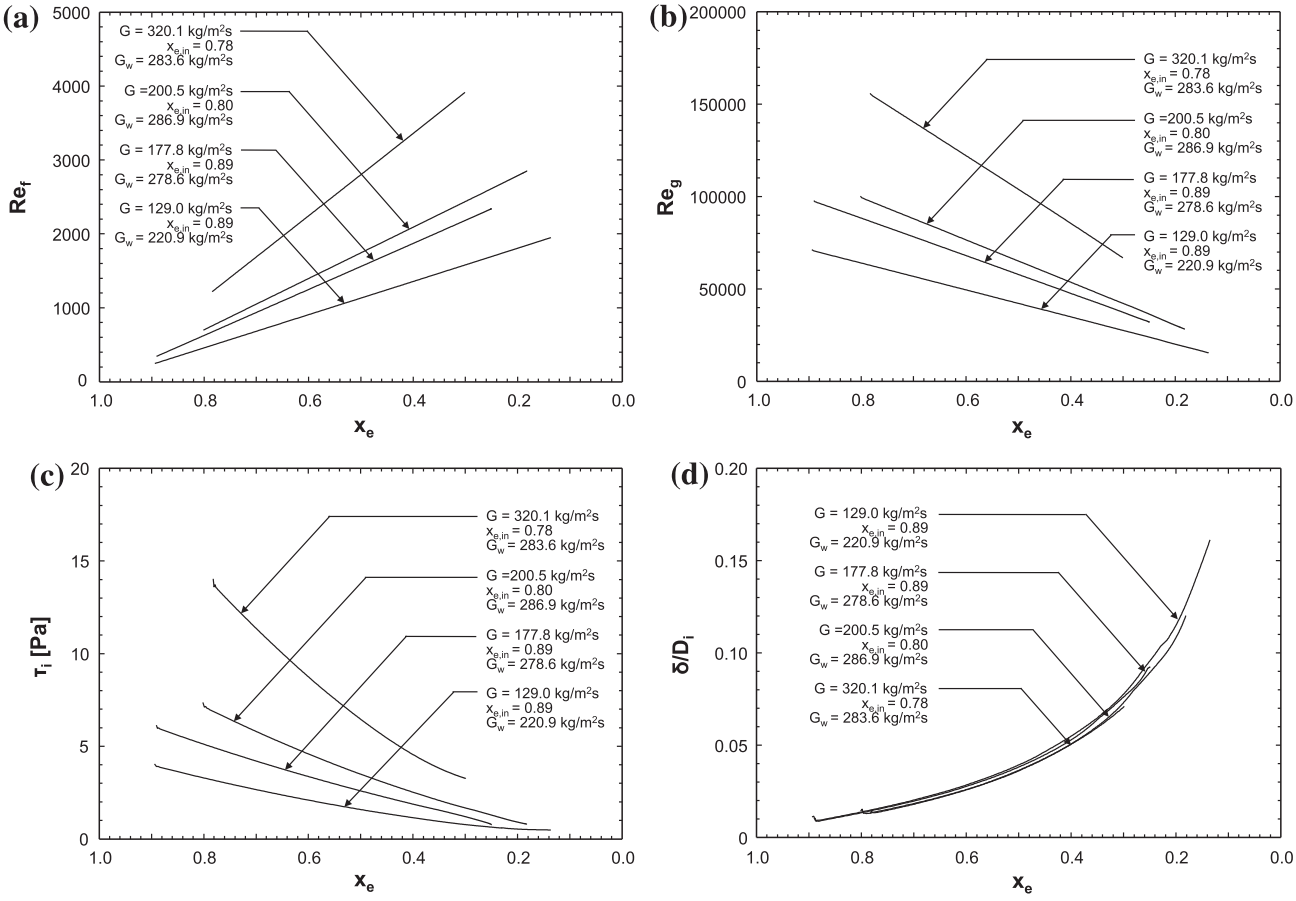

Fig. 13. Variations of predicted (a) liquid film Reynolds number, (b) vapor core Reynolds number, (c) interfacial shear stress and (d) liquid film thickness for different FC-72 and water mass velocities.

$K = 0.4$. The turbulent Prandtl number is obtained from a liquid film relation derived by Mudawar and El-Masri [48],

$$\mathrm{Pr}_{f,T} = 1.4\exp\left(-15\frac{y^+}{\delta^+}\right) + 0.66. \tag{6}$$

6. Model Predictions

Fig. 12(a)–(d) compares the axial variations of the experimentally-determined condensation heat transfer coefficient with the model predictions for four operating conditions. The model predicts the axially decreasing heat transfer coefficient with mean absolute errors (MAEs) ranging from 10.3% to 26.1%, where

$$\mathrm{MAE} = \frac{1}{N}\sum\left|\frac{\bar{h}_{pred} - \bar{h}_{\exp}}{\bar{h}_{\exp}}\right|. \tag{7}$$

Overall, the MAE for the entire database is 25.7%, with 60.5% and 97.4% of the data falling within ±30% and ±50%, respectively, from the model predictions. Most of the model error is associated with the upstream region, especially for high FC-72 mass velocity and relatively low inlet quality. This error may be attributed to the influence of liquid at the inlet that may be shattered away from the condensation tube and therefore not accounted for in the model. The shattered liquid decreases the inlet flow rate of the liquid film, resulting in a thinner film and the measured larger condensation heat transfer coefficient in the inlet region. Nonetheless, with an overall MAE of 25.7%, the present model constitutes an effective tool for predicting annular condensation in microgravity.

Aside from this influence, further enhancement of the model accuracy is possible by incorporating the influence of waves and a more accurate assessment of turbulence dampening near the film's interface. The influence of waves has been demonstrated for adiabatic [49,50], sensibly heated [51–53] and evaporating [54] falling liquid films. Ignoring the interfacial dampening of turbulent fluctuations due to surface tension can lead to substantial errors in predicting the condensation heat transfer coefficient [37].

Fig. 13(a)–(d) show the model predictions of the film's Reynolds number, Re_f, vapor core's Reynolds number, Re_g, interfacial shear stress, τ_i, and film thickness, δ, respectively, with thermodynamic equilibrium quality for four operating conditions. Re_f increases monotonically with decreasing x_e (increasing z), with the highest increase associated with the largest FC-72 mass velocity, which yields the highest interfacial shear and highest heat transfer coefficient. Because of mass conservation, Fig. 13(b) shows Re_g decreases monotonically with decreasing x_e. Fig. 13(c) shows τ_i decreases along the tube, with the highest FC-72 mass velocity yielding both the highest τ_i and fastest decrease in τ_i. Fig. 13(d) shows δ increases along the tube, with the smallest thickness achieved with the highest FC-72 mass velocity.

7. Conclusions

This study explored the development of an experimental facility for the study of annular flow condensation in microgravity in parabolic flight experiments as a prelude for development of NASA's Flow Boiling and Condensation Experiment (FBCE) for the International Space Station (ISS). Two separate condensation modules were tested using FC-72 as working fluid. The first, CM-HT, was dedicated to obtaining detailed heat transfer measurements, and the second, CM-FV, for video capture of the film's interface. The

measured condensation heat transfer coefficient was compared to predictions of a control-volume-based model. Key finding from the study are as follows:

(1) The interfacial character of the FC-72 condensation film is highly sensitive to the mass velocity of FC-72 and, to a far lesser degree, the mass velocity of the cooling water. At low FC-72 mass velocities, the film is laminar and the interface fairly smooth. Increasing the mass velocity causes the laminar film to turn quite wavy. At high mass velocities, the film turns turbulent, with the interface marred by both small ripples and fact moving large waves.
(2) The influence of gravity is very significant for low FC-72 mass velocities, where the film in microgravity is smooth-laminar and circumferentially uniform in thickness. For the same low mass velocity, Lunar gravity causes the film to thicken beneath the tube. The film thickening is even more severe in Martian gravity. However, the underside thickening is nonexistent in Lunar gravity and Martian gravity at high mass velocities because of the increased vapor shear stress on the film interface. An important practical conclusion concerning the implementation of condensation in space missions involving multiple gravity fields is that it is possible to negate the influence of gravity altogether by increasing the mass velocity of the working fluid.
(3) Heat transfer measurements show the condensation heat transfer coefficient is a strong function of the mass velocity of FC-72 and, to far lesser extent, the mass velocity of the cooling water. The condensation heat transfer coefficient is highest near the inlet, where the film is both thin and laminar, and decreases along the condensation length. This decrease is monotonic for low FC-72 mass velocities. However, high FC-72 mass velocities produce downstream enhancement that is attributed to both turbulence and increased waviness.
(4) A control-volume-based model of the condensation film, which accounts for dampening of turbulent fluctuations near the film interface, shows good agreement with the heat transfer coefficient data in both trend and magnitude, evidenced by an overall mean absolute error of 25.7%, with 60.5% and 97.4% of the data falling within ±30% and ±50%, respectively, of the model predictions. Suggestions are proposed for future enhancement of the model's accuracy.

Acknowledgements

The authors are grateful for the support of the National Aeronautics and Space Administration (NASA) under grant no. NNX13AB01G. The authors thank Rochelle May, Jeffrey Juergens, James Wagner, Nancy Hall, Henry Nahra, David Chao, Robert Butcher, Alban Seigneur, Bruce Frankenfield, Paul Trimarchi, Richard Kelsch, Daniel Gotti, Chip Redding, and Frank Kmiecik of the NASA Glenn Research Center, and Jeffrey Mackey of Vantage Partners LLC for their technical assistance.

References

[1] G. Ganapathi, G. Birur, E. Sunada, J. Miller, Two Phase vs Single Phase Thermal Loop Trades for Exploration Mission LAT II Architecture, SAE Technical Paper No. 01-1958, 2008.
[2] G. Ganapathi, G. Birur, G. Tsuyuki, R. Krylo, Mars Exploration Rover Heat Rejection System Performance–Comparison of Ground and Flight Data, SAE Technical Paper No. 01-2413, 2004.
[3] F.P. Chiaramonte, J.A. Joshi, Workshop on Critical Issues in Microgravity Fluids Transport and Reaction Processes in Advanced Human Support Technology, NASA Report TM-2004-212940, Washington, DC, 2004.
[4] H. Zhang, I. Mudawar, M.M. Hasan, Experimental assessment of the effects of body force, surface tension force, and inertia on flow boiling CHF, Int. J. Heat Mass Transfer 45 (2002) 4079–4095.
[5] H. Zhang, I. Mudawar, M.M. Hasan, A method for assessing the importance of body force on flow boiling CHF, ASME J. Heat Transfer 126 (2004) 161–168.
[6] H. Zhang, I. Mudawar, M.M. Hasan, Flow boiling CHF in microgravity, Int. J. Heat Mass Transfer 48 (2005) 3107–3118.
[7] T.M. Anderson, I. Mudawar, Microelectronic cooling by enhanced pool boiling of a dielectric fluorocarbon liquid, J. Heat Transfer Trans. ASME 111 (1989) 752–759.
[8] I. Mudawar, A.H. Howard, C.O. Gersey, An analytical model for near-saturated pool boiling CHF on vertical surfaces, Int. J. Heat Mass Transfer 40 (1997) 2327–2339.
[9] A.P. Ornatskii, L.S. Vinyarskii, Heat transfer crisis in a forced flow of underheated water in small-bore tubes, High Temp. 3 (1965) 400–406.
[10] T.C. Willingham, I. Mudawar, Forced-convection boiling and critical heat flux from a linear array of discrete heat sources, Int. J. Heat Mass Transfer 35 (1992) 2879–2890.
[11] D.D. Hall, I. Mudawar, Critical heat flux (CHF) for water flow in tubes-I. Compilation and assessment of world CHF data, Int. J. Heat Mass Transfer 43 (2000) 2573–2604.
[12] M. Monde, T. Inoue, Critical heat flux in saturated forced convective boiling on a heated disk with multiple impinging jets, J. Heat Transfer Trans. ASME 113 (1991) 722–727.
[13] D.C. Wadsworth, I. Mudawar, Enhancement of single-phase heat transfer and critical heat flux from an ultra-high-flux-source to a rectangular impinging jet of dielectric liquid, J. Heat Transfer Trans. ASME 114 (1992) 764–768.
[14] M.E. Johns, I. Mudawar, An ultra-high power two-phase jet-impingement avionic clamshell module, J. Electron. Packag. Trans. ASME 118 (1996) 264–270.
[15] S. Toda, A study in mist cooling (lst report: investigation of mist cooling), Trans. JSME 38 (1972) (1972) 581–588.
[16] J.R. Rybicki, I. Mudawar, Single-phase and two-phase cooling characteristics of upward-facing and downward-facing sprays, Int. J. Heat Mass Transfer 49 (2006) 5–16.
[17] W. Nakayama, T. Nakajima, S. Hirasawa, Heat sink studs having enhanced boiling surfaces for cooling of microelectronic components, ASME Paper No. 84-WA/HT-89, 1984.
[18] R.L. Webb, The evolution of enhanced surface geometries for nucleate boiling, Heat Transfer Eng. 2 (1981) 46–69.
[19] V. Khanikar, I. Mudawar, T. Fisher, Effects of carbon nanotube coating on flow boiling in a micro-channel, Int. J. Heat Mass Transfer 52 (2009) 3805–3817.
[20] The National Academies, Recapturing a Future for Space Exploration: Life and Physical Sciences Research for a New Era, National Academies Press, Washington, DC, 2011.
[21] European Space Agency (ESA), European Users Guide to Low Gravity Platforms, Noordwijk, Netherlands, 2005. UIC-ESA-UM-0001, Issue 2.
[22] N.J. Penley, C.P. Schafer, J.D.F. Bartoe, The international space station as a microgravity research platform, Acta Astronaut. 50 (2002) 691–696.
[23] W.W. Akers, H.A. Deans, O.K. Crosser, Condensing heat transfer within horizontal tubes, Chem. Eng. Prog. 54 (1958) 89–90.
[24] A. Cavallini, R. Zecchin, A dimensionless correlation for heat transfer in forced convection condensation, Proceedings of the 5th International Heat Transfer Conference, vol. 3, Tyoko, Japan, 1974, pp. 309–313.
[25] M.K. Dobson, J.C. Chato, Condensation in smooth horizontal tubes, J. Heat Transfer Trans. ASME 120 (1998) 193–213.
[26] K.W. Moser, R.L. Webb, B. Na, A new equivalent Reynolds number model for condensation in smooth tubes, J. Heat Transfer Trans. ASME 120 (1998) 410–417.
[27] Y.Y. Yan, T.F. Lin, Condensation heat transfer and pressure drop of refrigerant R-134a in a small pipe, Int. J. Heat Mass Transfer 42 (1999) 697–708.
[28] W.-W. Wang, T.D. Radcliff, R.N. Christensen, A condensation heat transfer correlation for millimeter-scale tubing with flow regime transition, Exp. Therm. Fluid Sci. 26 (2002) 473–485.
[29] S. Koyama, K. Kuwahara, K. Nakashita, K. Yamamoto, An experimental study on condensation of refrigerant R134a in a multi-port extruded tube, Int. J. Refrig. 24 (2003) 425–432.
[30] N.H. Kim, J.P. Cho, J.O. Kim, B. Youn, Condensation heat transfer of R-22 and R-410A in flat aluminum multi-channel tubes with or without micro-fins, Int. J. Refrig. 26 (2003) 830–839.
[31] X. Huang, G. Ding, H. Hu, Y. Zhu, H. Peng, Y. Gao, B. Deng, Influence of oil on flow condensation heat transfer of R410A inside 4.18 mm and 1.6 mm inner diameter horizontal smooth tubes, Int. J. Refrig. 33 (2010) 158–169.
[32] S.M. Kim, J. Kim, I. Mudawar, Flow condensation in parallel micro-channels–part 1: experimental results and assessment of pressure drop correlations, Int. J. Heat Mass Transfer 55 (2012) 971–983.
[33] S.M. Kim, I. Mudawar, Flow condensation in parallel micro-channels–part 2: heat transfer results and correlation technique, Int. J. Heat Mass Transfer 55 (2011) 984–994.
[34] M.M. Shah, A general correlation for heat transfer during film condensation inside pipes, Int. J. Heat Mass Transfer 22 (1979) 547–556.
[35] S.M. Kim, I. Mudawar, Universal approach to predicting two-phase frictional pressure drop for adiabatic and condensing mini/micro-channel flows, Int. J. Heat Mass Transfer 55 (2012) 3246–3261.
[36] S.M. Kim, I. Mudawar, Universal approach to predicting heat transfer coefficient for condensing mini/micro-channel flow, Int. J. Heat Mass Transfer 56 (2013) 238–250.

[37] S.M. Kim, I. Mudawar, Theoretical model for annular flow condensation in rectangular micro-channels, Int. J. Heat Mass Transfer 55 (2011) 958–970.
[38] I. Park, S.M. Kim, I. Mudawar, Experimental measurement and modeling of downflow condensation in a circular tube, Int. J. Heat Mass Transfer 57 (2013) 567–581.
[39] C.O. Cersey, I. Mudawar, Effects of heater length and orientation on the trigger mechanism for near-saturated flow boiling critical heat flux-I. Photographic study and statistical characterization of the near-wall interfacial features, Int. J. Heat Mass Transfer 38 (1995) 629–641.
[40] C.O. Cersey, I. Mudawar, Effects of heater length and orientation on the trigger mechanism for near-saturated flow boiling critical heat flux-II. Critical heat flux model, Int. J. Heat Mass Transfer 38 (1995) 643–654.
[41] J.C. Sturgis, I. Mudawar, Critical heat flux in a long, rectangular channel subjected to onesided heating-I. Flow visualization, Int. J. Heat Mass Transfer 42 (1999) 1835–1847.
[42] J.C. Sturgis, I. Mudawar, Critical heat flux in a long, rectangular channel subjected to onesided heating-II. Analysis of critical heat flux data, Int. J. Heat Mass Transfer 42 (1999) 1849–1862.
[43] G.B. Wallis, One-Dimensional Two-Phase Flow, McGraw-Hill, New York, 1969.
[44] R.K. Shah, A.L. London, Laminar Flow Forced Convection in Ducts: A Source Book for Compact Heat Exchanger Analytical Data, Academic Press, New York, 1978.
[45] E.R. Van Driest, On turbulent flow near a wall, J. Aeronaut. Sci. 23 (1956) 1007–1011.
[46] W.M. Kays, Heat transfer to the transpired turbulent boundary layer, Int. J. Heat Mass Transfer 15 (1972) 1023–1044.
[47] W.M. Kays, M.E. Crawford, Convective Heat and Mass Transfer, second ed., McGraw-Hill, New York, 1980.
[48] I. Mudawar, M. El-Masri, Momentum and heat transfer across freely-falling turbulent liquid films, Int. J. Multiphase Flow 12 (1986) 771–790.
[49] I. Mudawar, R.A. Houpt, Measurement of mass and momentum transport in wavy-laminar falling liquid films, Int. J. Heat Mass Transfer 36 (1993) 4151–4162.
[50] I. Mudawar, R.A. Houpt, Mass and momentum transport in smooth falling liquid films laminarized at relatively high Reynolds numbers, Int. J. Heat Mass Transfer 36 (1993) 3437–3448.
[51] J. Shmerler, I. Mudawar, Local heat transfer coefficient in wavy free-falling turbulent liquid films undergoing uniform sensible heating, Int. J. Heat Mass Transfer 31 (1988) 67–77.
[52] T. Lyu, I. Mudawar, Statistical investigation of the relationship between interfacial waviness and sensible heat transfer to a falling liquid film, Int. J. Heat Mass Transfer 34 (1991) 1451–1464.
[53] T. Lyu, I. Mudawar, Determination of wave-induced fluctuations of wall temperature and convection heat transfer coefficient in the heating of a turbulent falling liquid film, Int. J. Heat Mass Transfer 34 (1991) 2521–2534.
[54] J. Shmerler, I. Mudawar, Local evaporative heat transfer coefficient in turbulent free-falling liquid films, Int. J. Heat Mass Transfer 31 (1988) 731–742.